# A solid-polymer electrolyte direct methanol fuel cell with a mixed reactant and air anode

A.K. Shukla[1], C.L. Jackson, K. Scott[*], G. Murgia[2]

*Chemical and Process Engineering Department, University of Newcastle, Merz Court, Newcastle upon Tyne NE1 7RU, UK*

## Abstract

A comparison of the performance of a solid-polymer electrolyte direct methanol fuel cell (SPE-DMFC) with aqueous methanol and air mixed at the anode, and with only aqueous methanol is presented. The performance of the mixed methanol reactant and air fed anode SPE-DMFC is superior to the conventional methanol only fed anode SPE-DMFC. The experimental performance of the mixed-reactant anode SPE-DMFC are compared with results of a numerical modelling based on phenomenological transport equations for electrocatalyst layer, diffusion layer and the polymer electrolyte membrane.
© 2002 Published by Elsevier Science B.V.

*Keywords:* Mixed-reactant anode; Selective anode; Direct methanol fuel cell; Numerical modelling

## 1. Introduction

The direct use of methanol in fuel cells is considerably attractive from the point of view, of simplicity of system design and hence cost [1]. A direct methanol fuel cell (DMFC) consists of an anode at which methanol is electrochemically oxidised to carbon dioxide according to

$$CH_3OH + H_2O \rightarrow CO_2 \uparrow + 6H^+ + 6e^- \tag{1}$$
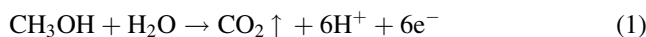
and a cathode at which oxygen is reduced to water

$$\tfrac{3}{2}O_2 + 6H^+ + 6e^- \rightarrow 3H_2O \tag{2}$$

Accordingly, the overall cell reaction is

$$CH_3OH + \tfrac{3}{2}O_2 \rightarrow CO_2 \uparrow + 2H_2O \tag{3}$$
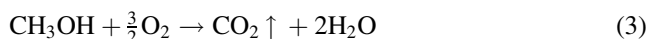
The present day DMFCs employ a thin proton-conducting polymer sheet as the electrolyte and hence are commonly referred to as solid polymer electrolyte direct methanol fuel cells (SPE-DMFCs). During the last decade, significant advances have been made in the DMFC development. Power densities of 450 and 300 mW/cm$^2$ under oxygen and air feed

operation, respectively, and 200 mW/cm$^2$ at a cell potential of 0.5 V have been reported for cells operating at temperatures close to or above 100 °C under pressurised conditions with platinum loadings of 1–2 mg/cm$^2$ [2,3]. Besides, the development of DMFC stacks for both transportation and portable, applications has gained momentum in the last 2–3 years, and stacks with power densities of 1 kW/dm$^3$ and an overall efficiency of 37% at a design point of 0.5 V per cell have been accomplished [4]. The performance of SPE-DMFCs is thus competitive with respect to the reformer-based H$_2$/air polymer electrolyte fuel cells (PEFCs), especially if one considers the complexity of the latter whole system [5]. In a recent review on the prospects of fuel cells for road-transportation purposes [6], it has been suggested that only fuel cell vehicles (FCVs) with directly fuelled fuel cells, such as the SPE-DMFCs, will be able to exceed the performance of future conventional internal combustion engine vechiles (ICEVs). However, further improvements in the anode performance of SPE-DMFCs in addition to a reduction in their cost would be mandatory for their use in FCVs [7]. A step in this direction appears to be the development of mixed-reactant SPE-DMFCs [8,9]. It is noteworthy that selective-electrode fuel cells with mixed-reactant feed have been considered for solid oxide [10] and proton-exchange membrane fuel cells [11,12].

In this communication, we report the performance of a SPE-DMFC with a mixed-reactant anode in conjunction with its numerical modelling. The study demonstrates that the SPE-DMFC with mixed-reactant anode exhibits superior

[*] Corresponding author. Tel.: +44-191-222-8771; fax: +44-191-222-5292.
*E-mail address:* k.scott@ncl.ac.uk (K. Scott).
[1] On leave from Solid State and Structural Chemistry Unit, Indian Institute of Science, Bangalore -560012, India.
[2] On leave from Center for Advanced Studies, Research and Development in Sardinia (CRS4), Uta, CA 09010, Italy.

**Nomenclature**

| | |
|---|---|
| $a$ | effective catalyst area per unit volume |
| $A_D$ | anode diffusion region |
| $A_R$ | anode reactive region |
| $c_i$ | concentration of species $i$ |
| $C_D$ | cathode diffusion region |
| $C_R$ | cathode reactive region |
| $D_i$ | diffusion coefficient of species $i$ |
| $D_{i-j}$ | pair diffusion coefficient of gas species $i$ and $j$ |
| $f$ | Faraday constant in units of $RT$ |
| $F$ | Faraday constant |
| $i_l$ | ionic current density |
| $i_s$ | electronic current density |
| $i_{0,ref}$ | exchange current density at reference conditions |
| $I$ | operative cell current density |
| $j$ | transfer current per unit volume |
| $k_p$ | hydraulic permeability |
| $k_\phi$ | electrokinetic permeability |
| $K_i$ | Henry's constant for species $i$ |
| $M$ | membrane region |
| $n$ | number of electrons |
| $N_i$ | mass flow of species $i$ |
| $P$ | pressure |
| $R$ | gas constant |
| $S_i$ | stoichiometric coefficient of species $i$ |
| $S_l$ | liquid saturation |
| $T$ | temperature |
| $v$ | water velocity |
| $x_i$ | molar fraction of species $i$ |
| $z$ | fixed-site charge |

*Greek symbols*

| | |
|---|---|
| $\alpha_a$ | anodic transfer coefficient |
| $\alpha_c$ | cathodic transfer coefficient |
| $\varepsilon_m$ | membrane porosity |
| $\varepsilon_p$ | diffusion region porosity |
| $\phi_l$ | electric potential of liquid phase |
| $\phi_s$ | electric potential of solid phase |
| $\gamma$ | kinetic factor |
| $\eta$ | interface overpotential |
| $\kappa$ | ionic conductivity |
| $\mu$ | water viscosity |
| $\rho$ | water density |
| $\sigma$ | electronic conductivity |

*Subscripts and superscripts*

| | |
|---|---|
| a | anode |
| av | average |
| c | cathode |
| eff | effective value |
| f | fixed-charge |
| g | gas phase |
| in | inlet |
| l | liquid phase |
| out | outlet |
| ref | reference conditions |
| sat | saturated vapor |
| w | water |

performance in relation to conventional selective-anode SPE-DMFCs.

## 2. Experimental

A SPE-DMFC was assembled with a Nafion®-117 based membrane electrode assembly (MEA) obtained from Johnson Matthey, which employed Pt-Ru/C as the anode catalyst with a loading of 1 mg/cm² of Pt and 0.46 mg/cm² of Ru, and Pt/C as the cathode catalyst with a loading of 4.6 mg/cm² of Pt. In the experimental cell, the anode and cathode of the MEA were in contact with high-density graphite blocks, impregnated with phenolic resin, into which were cut the gas/liquid flow channels [13]. The ridges between the channels provided the electrical contact to the carbon electrodes and the total machined geometrical area of 25 cm² was taken as the active area of the cell. Electrical heaters were mounted at the rear of the graphite blocks to maintain the desired cell temperature which was controlled through a temperature controller and monitored by thermocouples buried in the graphite blocks. Gold-plated metallic bolts were screwed into the blocks to allow electrical contact. For selective-anode tests, a solution of 1.0 mol/dm³ (M) aqueous methanol was fed to the anode at a feed rate of ca. 15 cm³/min and the unreacted fuel returned to the storage reservoir where the $CO_2$ gas product was released to the atmosphere. For the mixed-reactant anode test, either nitrogen gas or air pre-heated to cell temperature was fed at 200 cm³/min to the anode along with 1 M aqueous methanol.

On polarising the anode galvanostatically, hydrogen was evolved in accordance to the reaction:

$$6H^+ + 6e^- \rightarrow 3H_2 \uparrow \qquad (4)$$
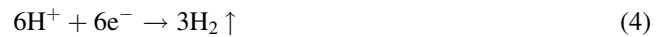
at the cathode which also served as a reference electrode [8,14]. To obtain the cell polarisation data, hot air at 200 cm³/min was also supplied to the cathode from an air cylinder. The experimental set-up employed for the study is shown schematically in Fig. 1.

## 3. Model description

The model uses a cell configuration comprising five regions as shown in Fig. 2, each of which has a different chemical and physical transport phenomenon. The model is primarily a modification of the approach described earlier for modelling a polymer electrolyte fuel cell [15–18]. In brief, the model uses a one-dimensional approach where the independent variables are the electrical potential of the solid
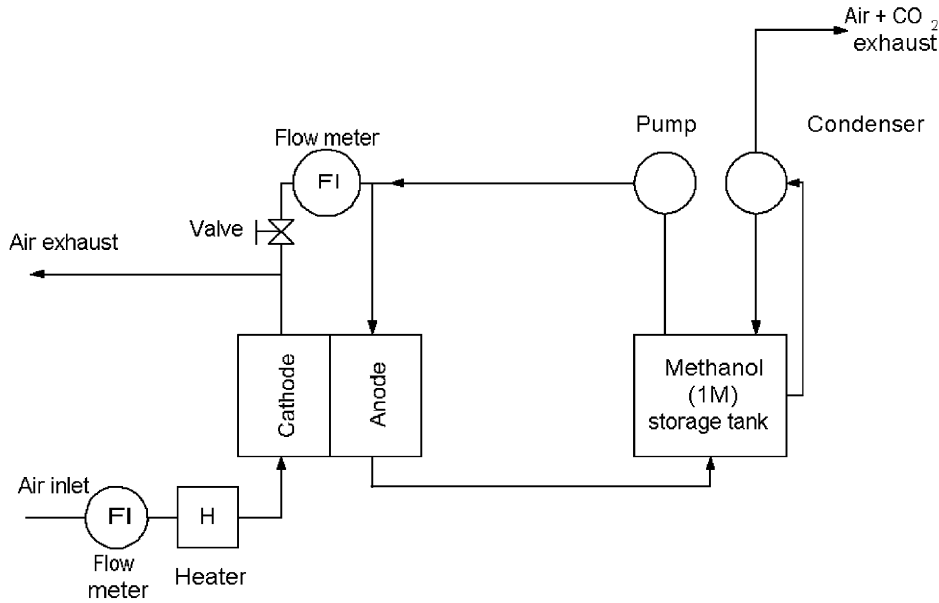
Fig. 1. Schematic diagram of the experimental set-up.

($\phi_s$) and liquid ($\phi_l$) phases, the hydraulic pressure ($P$), concentrations of methanol ($c_{CH_3OH}$), carbon dioxide ($c_{CO_2}$), and oxygen ($c_{O_2}$) in the liquid phase, and nitrogen molar fraction ($x_{N_2}$) in the gas phase. The modelled transport phenomena and conservation equations are in given in Table 1. Any spatial variation in the variables is governed by the respective phenomenological expressions, which relate the flux of any physical quantity to its generating force. The closed set of differential equations for the model, obtained by combining the phenomenological and conservation equations, are described in Table 2.

The model uses (a) the Stefan–Maxwell equation to account for gas-diffusion in porous medium, (b) the Nernst–Planck equation to account for the proton conduction and transport of the neutral chemical species in the electrolyte and the bulk-liquid phase, (c) Ohm's law for electronic conductivity in the bulk-solid phase, (d) a modified Schlögl equation [19,20] to account for convective motion in the membrane electrolyte and MEA comprising the backing plus diffusion layers where it takes the form of the Darcy equation. The model source equation for the reaction kinetics at the anode and cathode are obtained
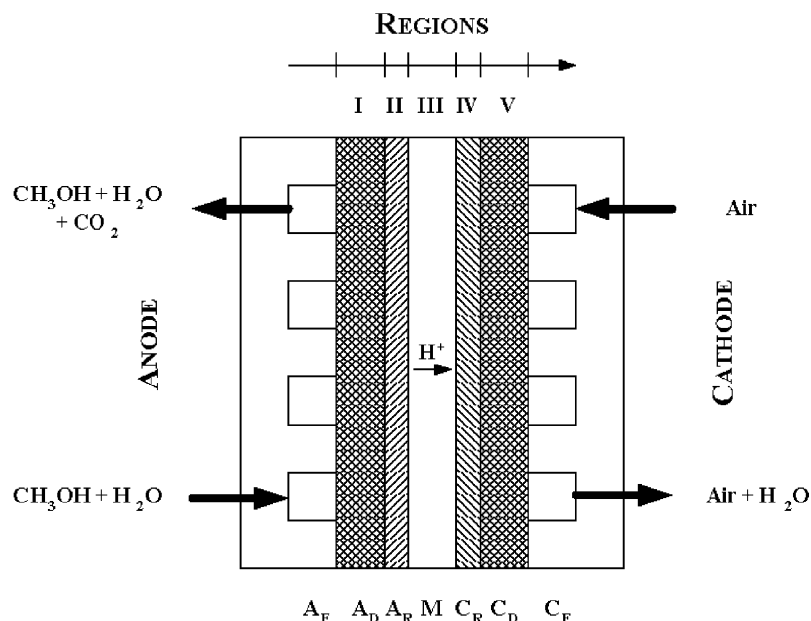


Fig. 2. Cell configuration adopted for numerical modelling.

**Table 1**
Model transport phenomena and its conservation equations

| Regions | Variables | Flux | Conservation |
|---|---|---|---|
| $A_D$ | $c_{CH_3OH}, c_{CO_2}, \phi_s, P$ | $N_{CH_3OH}, N_{CO_2}, i_s, v$ | $\nabla \cdot N_{CH_3OH} = \nabla \cdot N_{CO_2} = \nabla \cdot i_s = \nabla \cdot v = 0$ |
| $A_R$ | $c_{CH_3OH}, c_{CO_2}, \phi_s, \phi_1, P$ | $N_{CH_3OH}, N_{CO_2}, i_s, i_1, v$ | $\nabla \cdot N_{CH_3OH} = y_{CH_3OH}, \nabla \cdot N_{CO_2} = y_{CO_2}, \nabla \cdot i_s = -\nabla \cdot i_1 = j^a, \nabla \cdot v = \rho y_{H_2O}$ |
| $M$ | $c_{CH_3OH}, c_{O_2}, \phi_1, P$ | $N_{CH_3OH}, N_{O_2}, i_1, v$ | $\nabla \cdot N_{CH_3OH} = \nabla \cdot N_{O_2} = \nabla \cdot i_1 = \nabla \cdot v = 0$ |
| $C_R$ | $c_{CH_3OH}, c_{O_2}, \phi_s, \phi_1, P$ | $N_{CH_3OH}, N_{O_2}, i_s, i_1, v$ | $\nabla \cdot N_{O_2} = y_{O_2}, \nabla \cdot i_s = -\nabla \cdot i_1 = j^c, \nabla \cdot v = \rho y_{H_2O}$ |
| $C_D$ | $x_{N_2}, x_{O_2}, \phi_s, P$ | $N_{N_2}, N_{O_2}, i_s, v$ | $\nabla \cdot N_{N_2} = \nabla \cdot N_{O_2} = \nabla \cdot i_s = 0, \nabla \cdot v \propto \nabla \cdot N_{H_2O}$ |

In the table $y_i = (s_i^\beta / n^\beta F) j^\beta$, where $\beta = a, c$.

using Butler–Völmer equations, which assume the Tafel form for irreversible reactions, as described below.

$$\nabla \cdot i_a = a i_{0,a} \left( \frac{c_{CH_3OH}^a}{c_{CH_3OH}^{ref}} \right)^\gamma e^{\alpha_a f \eta_a} \tag{5}$$

where

$$f = \frac{F}{RT}; \quad \eta_a = \phi_{s,a} - \phi_{1,a}$$

and

$$\nabla \cdot i_c = a i_{0,c} \left( \frac{c_{O_2}^c}{c_{O_2}^{ref}} \right)^\gamma [-e^{\alpha_c f \eta_c}] \tag{6}$$

where

$$\eta_c = \phi_{s,c} - \phi_{1,c}$$

The other characteristics of the model assume (a) steady-state operation of the cell, (b) constant temperature (isothermal) operation of the cell, (c) zero differential gas pressure in the porous medium, (d) fully-hydrated electrolyte membrane, (e) variable gas–liquid saturation on the cathode, and (f) liquid-phase transport at the anode. Since the catalyst loading at the cathode is substantially high, any methanol crossover effect on the cathode polarisation has been neglected in the numerical modelling of the cell.

Since the present model is based on a mechanistic approach, it requires knowledge of several material properties, e.g. effective diffusion coefficients, hydraulic and electro-kinetic permeability, proton conductivity in the electrolyte, electronic conductivity in the electrodes, etc. These experimental parameters have been taken from the literature. Only electronic conductivity and the pre-exponential kinetic factor have been appropriately adjusted in the numerical modelling. Besides, the estimated effective values of all the transport coefficients account for the porosity of the medium under consideration. The generic effective diffusion and permeability coefficients, $k^{eff}$ and $D^{eff}$, respectively, for various reactant/product species in the membrane electrolyte are obtained by,

$$k^{eff} = k \varepsilon_m \tag{7}$$

**Table 2**
System of coupled differential equations for the numerical modelling

| Variables | Equations | Validity Regions | Phenomenological equation |
|---|---|---|---|
| $c_{CH_3OH}$ | $\nabla \cdot (D_{CH_3OH} \nabla c_{CH_3OH} - c_{CH_3OH} v) = 0$ | $M$ | Nernst–Planck |
| | $\nabla \cdot (D_{CH_3OH} \nabla c_{CH_3OH} - c_{CH_3OH} v) = y_{CH_3OH}$ | $A_D$ | |
| $c_{CO_2}$ | $\nabla \cdot (D_{CO_2} \nabla c_{CO_2} - c_{CO_2} v) = 0$ | $M$ | Nernst–Planck |
| | $\nabla \cdot (D_{CO_2} \nabla c_{CO_2} - c_{CO_2} v) = y_{CO_2}$ | $A_D$ | |
| $c_{O_2}$ | $\nabla \cdot (D_{O_2} \nabla c_{O_2} - c_{O_2} v) = 0$ | $M$ | Nernst–Planck |
| | $\nabla \cdot (D_{O_2} \nabla c_{O_2} - c_{O_2} v) = y_{CO_2}$ | $C_D$ | |
| $x_{N_2}$ | $\nabla x_{N_2} = \sum_{j=1}^n (RT/PD_{N_2-j})(x_{N_2} N_j - x_j N_{N_2})$ where $j = O_2, H_2O$ | $C_D$ | Stefan–Maxwell |
| $x_{O_2}$ | $\nabla x_{O_2} = \sum_{j=1}^n (RT/PD_{O_2-j})(x_{O_2} N_j - x_j N_{O_2})$ where $j = N_2, H_2O$ | $C_D$ | Stefan–Maxwell |
| $\phi_s$ | $\nabla \cdot (\sigma \nabla \phi_s) = 0$ | $M$ | Ohm's law |
| | $\nabla \cdot (\sigma \nabla \phi_s) = j^a$ | $C_A$ | |
| | $\nabla \cdot (\sigma \nabla \phi_s) = j^c$ | $C_D$ | |
| $\phi_1$ | $\nabla \cdot (\kappa \nabla \phi_1 + F c_f \varepsilon v) = 0$ | $M$ | Nernst–Planck |
| | $\nabla \cdot (\kappa \nabla \phi_1 + F c_f \varepsilon v) = j^a - (F c_f / \rho) y_{H_2O}$ | $C_A$ | |
| | $\nabla \cdot (\kappa \nabla \phi_1 + F c_f \varepsilon v) = j^c - (F c_f / \rho) y_{H_2O}$ | $C_D$ | |
| $P$ | $\nabla \cdot (-(k_P/\mu) \nabla P) = 0$ | $A_D, C_D$ | Darcy |
| | $\nabla \cdot (b \nabla \phi_1 - (k_P/\mu) \nabla P) = 0$ | $M$ | Modified Schlögl |
| | $\nabla \cdot (b \nabla \phi_1 - (k_P/\mu) \nabla P) = -(1/\rho) y_{H_2O}$ | $C_A$ | |
| | $\nabla \cdot (b \nabla \phi_1 - (k_P/\mu) \nabla P) = -(1/\rho) y_{H_2O}$ | $C_D$ | |

In the table $b = (k_\phi / \mu) z_f c_f F$.

and

$$D^{\text{eff}} = D\varepsilon_{\text{m}} \qquad (8)$$

where $\varepsilon_{\text{m}}$ is the membrane fraction in the catalyst layer.

In the porous region, the total porosity ($\varepsilon_{\text{p}}$) may be partially occupied by water and gas and therefore, we need to specify the relative occupancy of either phase while accounting for the effective diffusion and permeability coefficients at the anode and cathode. In the electrode porous region, the Bruggemann correction to the diffusion coefficients is applied for porous systems with homogeneous porosity and particle size [21].

Accordingly, at the anode,

$$D^{\text{eff}} = D(\varepsilon_{\text{p}}^{\text{l}})^{1.5} \qquad (9)$$

where $\varepsilon_{\text{p}}^{\text{l}} = \varepsilon_{\text{p}}S_{\text{l}}$, $S_{\text{l}}$ being the liquid-phase saturation parameter. Similarly, at the cathode,

$$D^{\text{eff}} = D(\varepsilon_{\text{p}}^{\text{g}})^{1.5} \qquad (10)$$

where $\varepsilon_{\text{p}}^{\text{g}} = \varepsilon_{\text{p}}(1 - S_{\text{l}})$. The hydraulic permeability ($k_{\text{p}}$) accounts for changes in liquid saturation in accordance with the equation [22,23]

$$k_{\text{p}}^{\text{eff}} = k_{\text{p}}S_{\text{l}}^3 \qquad (11)$$

The full set of model parameters is given in Table 3.

Table 3
Model parameters employed in the numerical modelling

| Parameters | Values | Reference |
|---|---|---|
| **Physical and operative parameters** | | |
| Membrane thickness | 230 µm | |
| Diffusive region thickness | 260 µm | |
| Catalyst layer thickness | 10 µm | |
| Cell temperature ($T$) | 80 °C | |
| Anode inlet pressure $P_{\text{a}}^{\text{in}}$ | 1 atm | |
| Cathode inlet pressure $P_{\text{c}}^{\text{in}}$ | 1 atm | |
| Nitrogen–oxygen mole ratio | 0.79/0.21 | |
| Anode feed flow rate (liquid) | 15 ml/min | |
| Cathode feed flow rate (gas) | 200 ml/min | |
| **Membrane parameters** | | |
| Ionic conductivity ($\kappa$) | 0.14 mho/cm | [25] |
| $CH_3OH$ diffusivity ($D_{CH_3OH}$) | $2.59 \times 10^{-6}$ cm²/s | [25] |
| $CO_2$ diffusivity ($D_{CO_2}$) | $2.5 \times 10^{-6}$ cm²/s | |
| $O_2$ diffusivity ($D_{O_2}$) | $1.22 \times 10^{-6}$ cm²/s | [26] |
| Fixed charge concentration ($c_{\text{f}}$) | $1.2 \times 10^{-3}$ mol/cm³ | [18] |
| $O_2$ Henry's constant ($K_{O_2}$) | $2.02 \times 10^5$ atm cm³/mol | [26] |
| Hydraulic permeability ($k_{\text{p}}$) | $1.8 \times 10^{-14}$ cm² | [18] |
| Electrokinetic permeability ($k_{\phi}$) | $7.18 \times 10^{-16}$ cm² | [18] |
| Water viscosity ($\mu$) | $4.56 \times 10^{-4}$ kg/m s | [27] |
| Water density ($\rho$) | 0.054 mol/cm³ | [27] |
| **Electrode parameters** | | |
| Electronic conductivity ($\sigma$) | 0.38 mho/cm | |
| $CH_3OH$ diffusivity (in water, $D_{CH_3OH}$) | $8.5 \times 10^{-5}$ cm²/s | [28] |
| $CO_2$ diffusivity (in water, $D_{CO_2}$) | $3.5 \times 10^{-5}$ cm²/s | |
| $O_2$–$N_2$ pressure–diffusivity ($D_{O_2-N_2}$) | 0.279 atm cm²/s | [18] |
| $O_2$–$H_2O$ pressure–diffusivity ($D_{O_2-H_2O}$) | 0.370 atm cm²/s | [18] |
| $H_2O$–$N_2$ pressure–diffusivity ($D_{H_2O-N_2}$) | 0.387 atm cm²/s | [18] |
| Membrane fraction in catalyst layer ($\varepsilon_{\text{m}}$) | 0.4 | [18] |
| Diffuser layer porosity ($\varepsilon_{\text{p}}$) | 0.4 | [18] |
| Liquid saturation in anode ($S_{\text{l}}$) | 0.75 mixed-reactants feed, 0.50 selective-reactant feed | |
| Electrokinetic permeability ($k_{\phi}$) | $7.18 \times 10^{-16}$ cm² | [18] |
| **Kinetics parameters** | | |
| Pre-exponential parameter ($ai_{0,\text{ref}}$) | $2.6 \times 10^{-1}$ A/cm³ anode, $2.0 \times 10^{-4}$ A/cm³ cathode | |
| Cathodic transfer coefficient ($\alpha_{\text{c}}$) | 1.2 for oxygen reduction | [16] |
| Anodic transfer coefficient ($\alpha_{\text{a}}$) | 0.5 for methanol oxidation | [29] |
| $O_2$ reference concentration ($c_{O_2,\text{ref}}$) | $4.72 \times 10^{-7}$ mol/cm³ | |
| $CH_3OH$ concentration ($c_{CH_3OH,\text{ref}}$) | $1.0 \times 10^{-3}$ mol/cm³ | |
| $O_2$ concentration parameter ($\gamma_{O_2}$) | 1.0 | [16] |
| $CH_3OH$ concentration parameter ($\gamma_{CH_3OH}$) | 1.0 | [29] |
| $CH_3OH$ stoichiometric coefficient ($s_{CH_3OH}$) | 1 | |
| $CO_2$ stoichiometric coefficient ($s_{CO_2}$) | −1 | |
| $H_2O$ stoichiometric coefficient ($s_{H_2O}$) | 1 anode, 3 cathode | |
| $O_2$ stoichiometric coefficient ($s_{O_2}$) | −3/2 | |
| Number of electrons ($n$) | 6 | |

**Table 4**
Internal boundary conditions for the system of coupled differential equations

| | $A_D/A_R$ | $A_R/M$ | $M/C_R$ | $C_R/C_D$ |
|---|---|---|---|---|
| $c_{CH_3OH}$ | $D_{CH_3OH}\nabla c_{CH_3OH}\vert_- =$ $D_{CH_3OH}\nabla c_{CH_3OH}\vert_+$ | $D_{CH_3OH}\nabla c_{CH_3OH}\vert_- =$ $D_{CH_3OH}\nabla c_{CH_3OH}\vert_+$ | $D_{CH_3OH}\nabla c_{CH_3OH}\vert_- =$ $D_{CH_3OH}\nabla c_{CH_3OH}\vert_+$ | $c_{CH_3OH}\vert_- = 0$ |
| $c_{CO_2}$ | $D_{CO_2}\nabla c_{CO_2}\vert_- =$ $D_{CO_2}\nabla c_{CO}\vert_+$ | $c_{CO_2}\vert_- = 0$ | – | – |
| $c_{O_2}$ | – | $c_{O_2}\vert_+ = 0$ | $D_{O_2}\nabla c_{O_2}\vert_- = D_{O_2}\nabla c_{O_2}\vert_+$ | $c_{O_2}\vert_+ = x_{O_2}\vert_+ P^{in}/K_{O_2}$ |
| $x_{N_2}$ [a] | – | – | – | – |
| $x_{O_2}$ [a] | – | – | – | – |
| $\phi_s$ | $\sigma\nabla\phi_s\vert_- = \sigma\nabla\phi_s\vert_+$ | $\nabla\phi_s\vert_- = 0$ | $\nabla\phi_s\vert_+ = 0$ | $\sigma\nabla\phi_s\vert_- = \sigma\nabla\phi_s\vert_+$ |
| $\phi_1$ | $\phi_1\vert_+ = 0$ | $\kappa\nabla\phi_1\vert_- = \kappa\nabla\phi_1\vert_+$ | $\kappa\nabla\phi_1\vert_- = \kappa\nabla\phi_1\vert_+$ | $\kappa\nabla\phi_1\vert_- = Fc_f\varepsilon_m v\vert_-$ |
| $P$ | $(N_{H_2O}/\rho) - (k_P/\mu)\nabla P\vert_- =$ $b\nabla\phi_1\vert_+ - (k_P/\mu)\nabla P\vert_+$ | $b\nabla\phi_1\vert_- - (k_P/\mu)\nabla P\vert_- =$ $b\nabla\phi_1\vert_+ - (k_P/\mu)\nabla P\vert_+$ | $b\nabla\phi_1\vert_- - (k_P/\mu)\nabla P\vert_- =$ $b\nabla\phi_1\vert_+ - (k_P/\mu)\nabla P\vert_+$ | $b\nabla\phi_1\vert_- - (k_P/\mu)\nabla P\vert_- =$ $(N_{H_2O}/\rho) - (k_P/\mu)\nabla P\vert_+$ |

In the table $b = (k_\phi/\mu)z_f c_f F$; the subscripts $-$ and $+$ refer to the regions on the left and on the right of the interface, respectively.

[a] The boundary conditions are given at the $C_D/C_F$ interface.

Solution of the numerical model is obtained once a proper set of boundary condition is given. For one-dimensional models, where cell inlet and outlet are coincident, the task is not trivial and a number of assumptions, valid for the system under consideration, are desired. For example, in the cell, we assume that hydraulic inlet pressure equals its outlet pressure, i.e. $P^{in} = P^{out}$. Besides, for the chemical species concentration, it is mandatory to obtain a mass balance between the inlet and outlet compositions of the reactants/products. While the inlet compositions are known, the outlet compositions are unknown a priory. Therefore,

$$c^{av} = \tfrac{1}{2}(c_i^{in} + c_i^{out}) \tag{12}$$

has to be estimated by an iterative procedure which yields self-consistent values for $c_i^{out}$ and its flux $N_i^{out}$. For the liquid-phase transport at the anode side,

$$c_{i,a}^{out} = \frac{c_{w,a}N_{i,a}^{out}}{N_{w,a}^{out}} \tag{13}$$

where $c_{w,a}$ is the water concentration assumed to be constant as water is the excess solvent, $N_{i,a}^{out}$ and $N_{w,a}^{out}$ are the outlet flux of the species $i$ and water, respectively. Similarly, for the gas-phase transport at the cathode side, the molar fraction of the species at the outlet is,

$$x_{i,c}^{out} = \frac{N_{i,c}^{out}}{\sum_i N_{i,c}^{out}} \tag{14}$$

Further details on mass balance for fuel cell systems can be found elsewhere [24]. The cathode solid-phase potential in the catalyst–diffuser region interface is obtained by using

$$\phi_s = \phi_1 - \frac{1}{\alpha_c f}\left\{2\ln(I) - \ln\left(\frac{2nFD_{O_2}}{s_{O_2}(\gamma_{O_2}+1)}ai_{0,c,ref}c_{O_2,ref}\right) - (\gamma_{O_2}+1)\ln\left(\frac{c_{O_2}^{C_D/C_R}}{c_{O_2,ref}^{C_D/C_R}}\right)\right\} \tag{15}$$

derived by an approximate analytical integration of the Butler–Völmer equation over the entire catalyst layer volume [15]. The approximations applied for the Butler–Völmer equation integration at the cathode side are not valid at the anode. Therefore, we are not able to write an explicit relation for the potential at the catalyst–diffuser region interface and an iterative optimisation procedure is required to obtain its value. For the liquid-phase potential, an arbitrary value can be given at the anode catalyst–diffuser region interface. The internal boundary conditions employed to couple the five numerical regions and to solve the entire set of equations are given in Table 4.

## 4. Results and discussion

The galvanostatic polarisation data for the selective and mixed-reactants anode tests are given in Fig. 3. Unlike the data reported by Barton et al. [8] for their mixed-reactant, strip-cell DMFC, we find a substantial improvement in the performance of the anode particularly at load current densities beyond ∼400 mA/cm². But, akin to the findings of Barton et al. [8], we also observe little difference between the anode polarisation data obtained with the mixed feed of 1 M aqueous methanol plus air, and the anode polarisation data obtained with 1 M aqueous methanol plus nitrogen. These data clearly reflect that the added oxygen does not lead to any significant parasitic-oxidation of methanol at the anode. Besides, unlike the observation of Barton et al. [8], we do not find the air stream to impede the mass transfer of methanol to the anode surface. Instead, we observe that air-feed helps scavenge carbon dioxide from the active catalytic sites ameliorating oxidation of methanol on the anode.

It is worth noting that a SPE-DMFC operating at 1 A load would require $5.8 \times 10^{-5}$ dm³/s of oxygen at the cathode, and $7.06 \times 10^{-8}$ dm³/s of methanol at the anode, and will result in water production of $6.26 \times 10^{-8}$ dm³/s at the cathode and $CO_2$ exhaust of $3.87 \times 10^{-5}$ dm³/s at its anode.
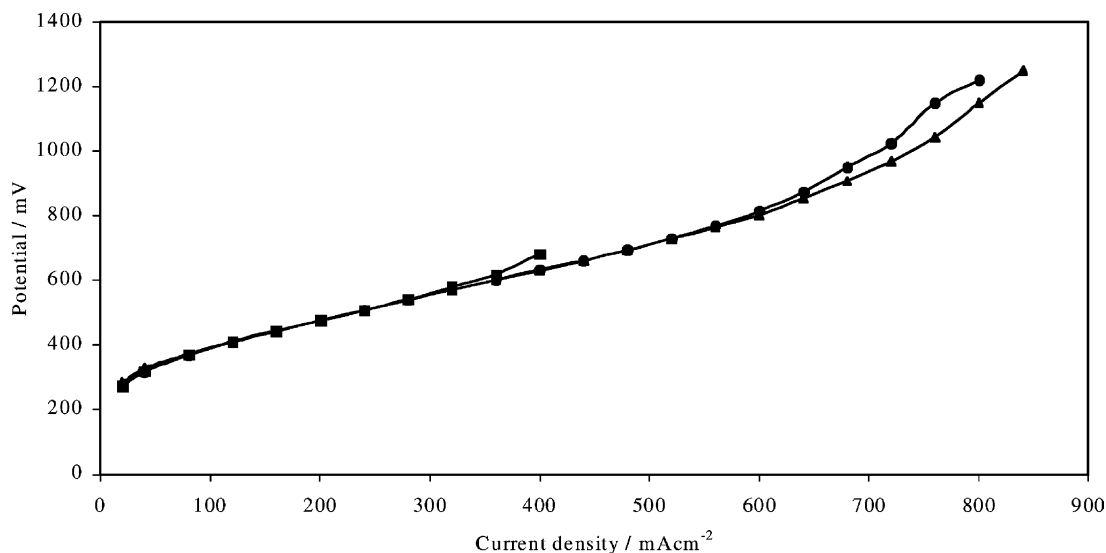
Fig. 3. Anode polarisation data obtained at 80 °C for (■) selective anode with 1 M aqueous methanol at feed rate of ca. 15 cm$^3$/min, (●) mixed-reactant anode with 1 M methanol at feed rate of ca. 15 cm$^3$/min plus 200 ml/min air at atmospheric pressure, and (▲) mixed-reactant anode with 1 M methanol at feed rate of ca. 15 cm$^3$/min plus 200 cm$^3$/min nitrogen at atmospheric pressure.

This represents ca. 550-fold volume increase in the anode compartment of the cell during its operation and suggests that efficient $CO_2$ removal from the anode would be seminal to further the cell performance.

Galvanostatic polarisation data for the complete cell are given in Fig. 4. A high catalyst loading of 4.8 mg/cm$^2$ of Pt on the cathode was used intentionally to minimise the cathode losses owing to any methanol crossover from the anode to the cathode. The data clearly suggest that the cell performance with mixed-feed anode to be superior in relation to its polarisation data for the methanol only fed anode.

The polarisation plots obtained from the numerical modelling of the SPE-DMFC, its anode, both with selective and mixed-reactant configurations, and its cathode are given in Figs. 5–7. A comparison of the anode polarisation data obtained from the experiments (Fig. 3) and modelling (Fig. 6) suggests them to be in conformity. The only parameter that differs in the numerical modelling of the polarisation data for the selective and mixed-reactant anodes is the liquid saturation ($S_l$) in the diffusion layer of the anode which has the relative values of 0.5 and 0.75, respectively. In the mixed-reactant anode, carbon dioxide evolving at the
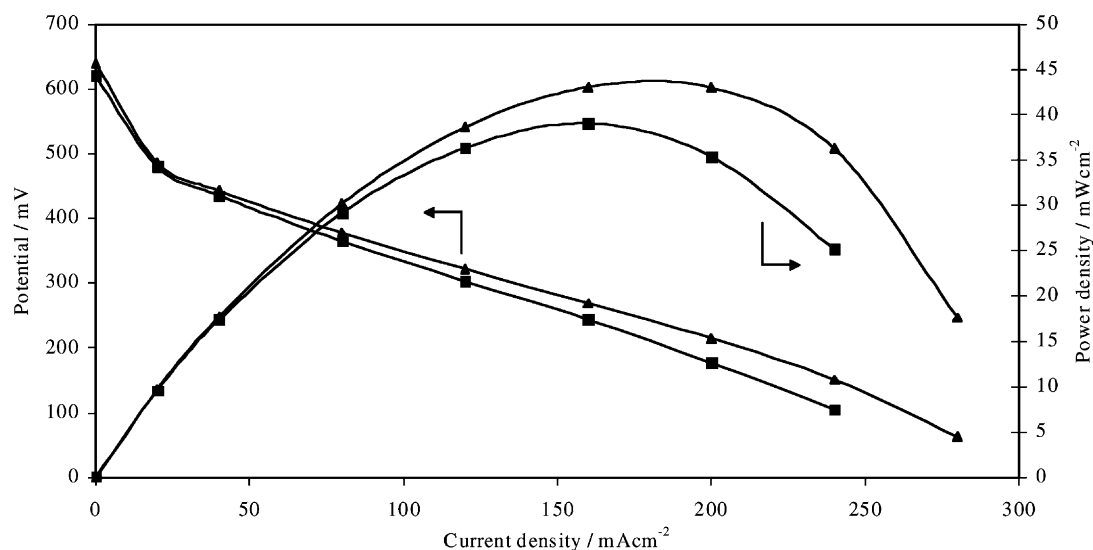


Fig. 4. Cell polarisation data obtained at 80 °C for (■) selective anode with 1 M aqueous methanol at feed rate of ca. 15 cm$^3$/min and cathode air flow rate of 200 cm$^3$/min at atmospheric pressure, and (▲) mixed-reactant anode with 1 M methanol at feed rate of ca. 15 cm$^3$/min plus 200 cm$^3$/min air at atmospheric pressure and cathode air feed at 200 cm$^3$/min at atmospheric pressure.
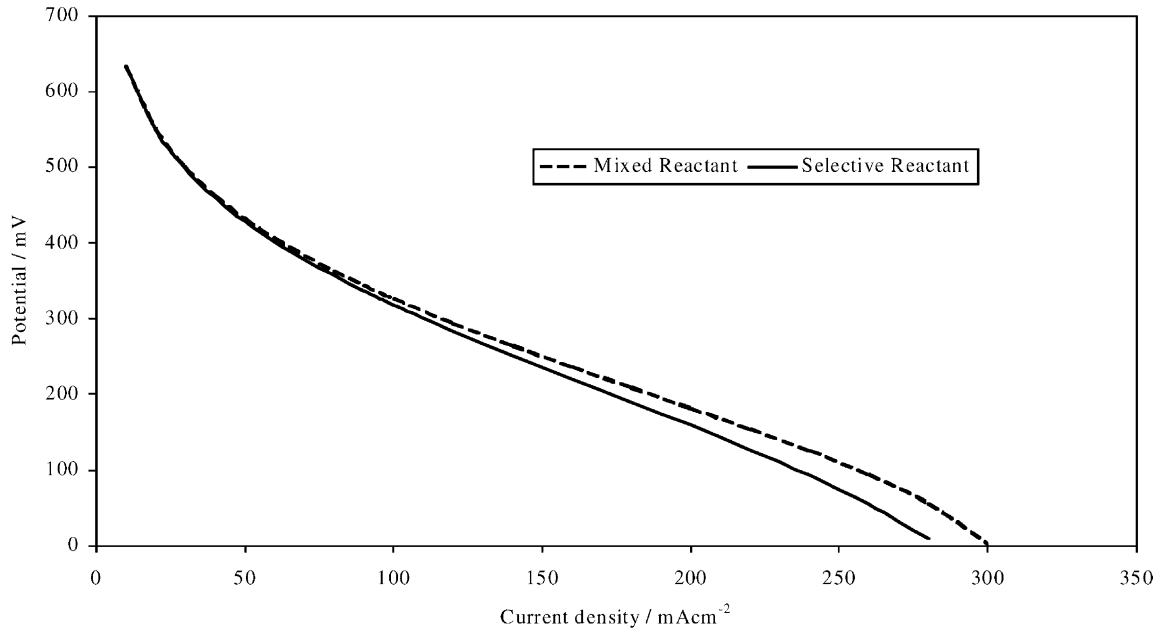
Fig. 5. Numerical modelling for polarisation of the SPE-DMFC with selective and mixed-reactant anodes akin to the experimental conditions.

anode will be easily removed from the electrode pores, as it will readily mix with the air stream. By contrast, in the selective-reactant anode, evolving carbon dioxide will register a back-pressure in the electrode pores due to the liquid stream in the flow field which will hinder its escape from the pores. Thus, a reduction in the liquid-saturation parameter will obstruct the effective supply of methanol to the electrode surface bringing about its polarisation much earlier in relation to the mixed-reactant anode.

From the numerical modelling of the air cathode (Fig. 7), the presence of an excessive amount of saturated water vapour ($x_w^{sat}$) in electrode pores in the air cathode at 80 °C and 1 atm of air seems to be the limiting factor for its performance. This suggests that an increase in either the flow rate of the air feed at the cathode or its pressure will be mandatory to further the performance of the SPE-DMFC. There is no reason to believe that the cell engineering and its operating conditions are yet fully
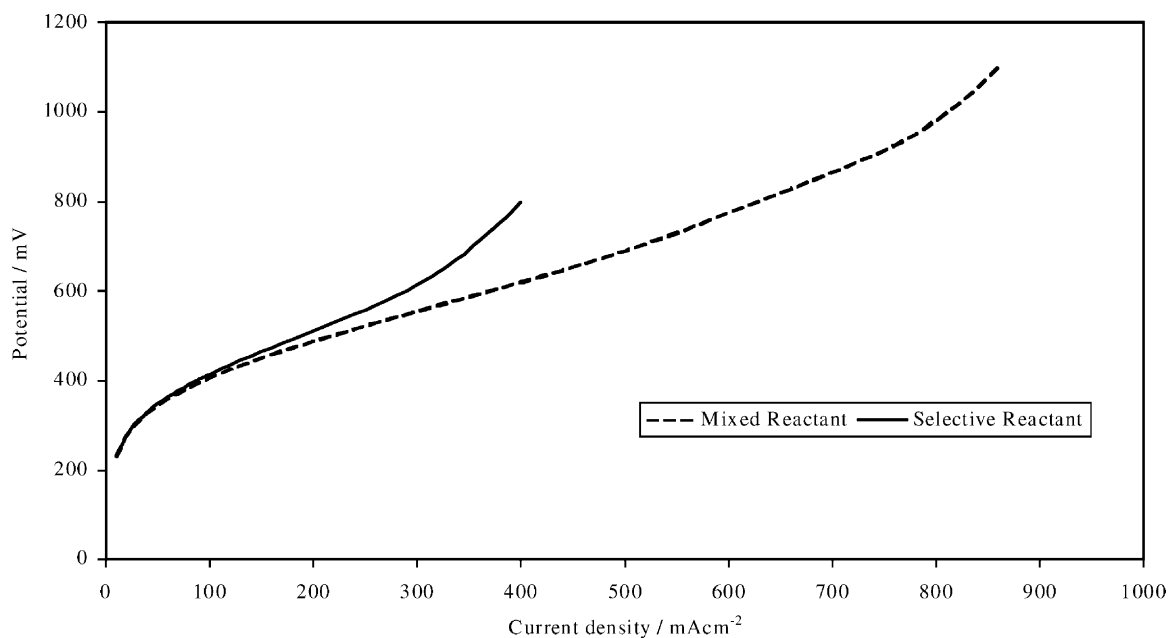


Fig. 6. Numerical modelling of the anode polarisation for selective and mixed-reactant anodes akin to the experimental conditions.
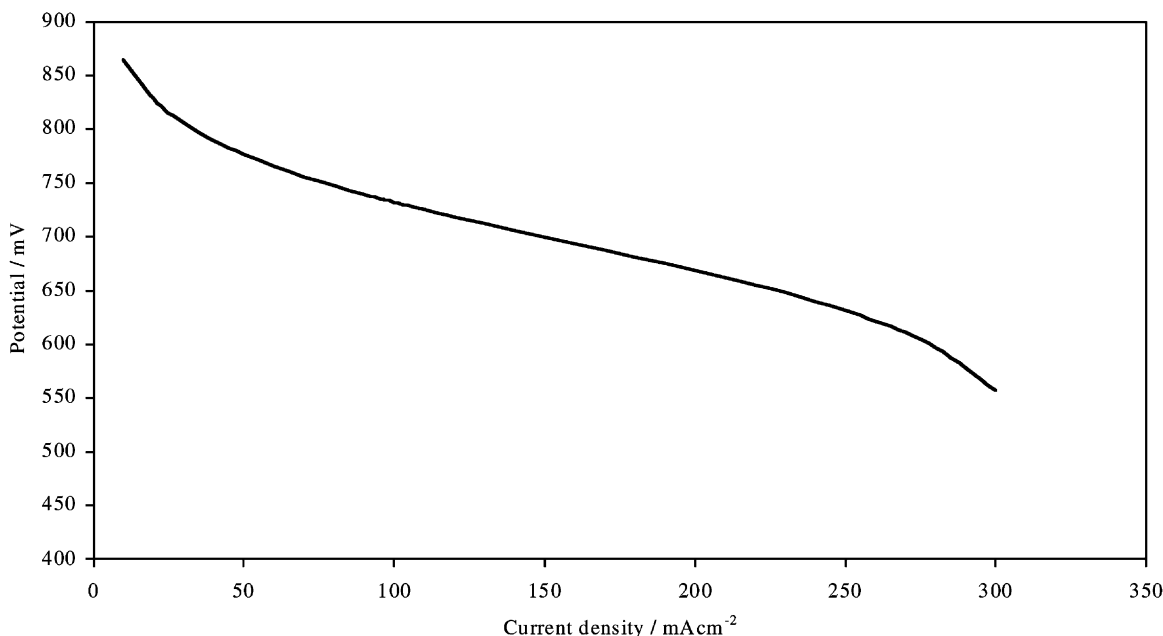
Fig. 7. Numerical modelling of the air-cathode polarisation at air-feed rate of 200 cm$^3$/min at atmospheric pressure akin to the experimental conditions.

optimised, and further improvements in the cell performance are highly likely.

## 5. Conclusions

This study has shown that using a mixed air and methanol solution anode stream in the DMFC leads to an increase in anode and cell performance. It is suggested that this improvement is due to a higher liquid saturation in the anode diffusion layer of the DMFC and the faster removal of carbon dioxide at its anode.

## Acknowledgements

## References

[1] A. Hamnett, Phil. Trans. Roy. Soc. London A354 (1996) 1653.
[2] A.S. Aricò, S. Srinivasan, V. Antonucci, Fuel Cells 1 (2001) 1.
[3] C. Lamy, A. Lima, V. LeRuhn, F. Delime, C. Coutanceau, J.-M. Léger, J. Power Sources 105 (2002) 283.
[4] X. Ren, P. Zelenay, S. Thomas, J. Davey, S. Gottesfeld, J. Power Sources 86 (2000) 111.
[5] A.K. Shukla, A.S. Aricò, V. Antonucci, Renew. Sustain. Ener. Rev. 5 (2001) 137.
[6] B.D. McNicol, D.A.J. Rand, K.R. Williams, J. Power Sources 100 (2001) 47.
[7] G.J.K. Acres, J. Power Sources 100 (2001) 60.
[8] S.C. Barton, T. Patterson, E. Wang, T.F. Fuller, A.C. West, J. Power Sources 96 (2001) 329.
[9] M.A. Priestnall, V.P. Kotzeva, D.J. Fish, J. Power Sources 106 (2002) 21.
[10] K. Asano, H. Iwahara, J. Electrochem. Soc. 144 (1997) 3125.
[11] G.A. Louis. J.M. Lee, D.L. Maricle, J.C. Trocciola, US Patent 4,248,941 (1981).
[12] C.K. Dyer, Nature 343 (1990) 547.
[13] M. Neergat, Ph.D. Thesis, Indian Institute of Science, Bangalore, India, 2001.
[14] N. Miyake, J.S. Wainright, R.F. Savinell, J. Electrochem. Soc. 148 (2001) 905.
[15] G. Murgia, L. Pisani, M. Valentini, B. D'Aguanno, J. Electrochem. Soc. 149 (2002) A31.
[16] L. Pisani, G. Murgia, M. Valentini, B. D'Aguanno, J. Electrochem. Soc., in press.
[17] D.M. Bernardi, M.W. Verbrugge, AIChE J. 37 (1991) 1151.
[18] D.M. Bernardi, M.W. Verbrugge, J. Electrochem. Soc. 139 (1992) 2477.
[19] R. Schlögl, Z. Physik. Chem. 3 (1955) 73.
[20] R. Schlögl, Ber. Bunsenges. Phys. Chem. 70 (1966) 400.
[21] R.E. De la Rue, C.W. Tobias, J. Electrochem. Soc. 106 (1959) 827.
[22] J. Bear, Dynamics of Fluids in Porous Media, Dover, New York, 1960.
[23] C.Y. Wang, Numerical Heat Transfer B Fundam. 31 (1997) 85.
[24] P.S. Kauranen, Thesis, Helsinki University of Technology, Finland, 1996.
[25] K. Scott, W. Tama, J. Kruickshank, J. Power Sources 65 (1997) 159.
[26] Z. Ogumi, Z. Takehara, S. Yoshizawa, J. Electrochem. Soc. 131 (1984) 769.
[27] CRC Handbook of Chemistry and Physics, CRC Press, Ohio, 2000.
[28] X. Ren, T.A. Zawodzinski Jr., F. Uribe, H. Dai, in: S. Gottesfeld, G. Halpert, A. Landgrebe (Eds.), Proceedings of the First International Symposium on Proton Conducting Fuel Cells I, Vol. 95-23, 10 South Main Street, Pennington, NJ, 1995, pp. 284–298.
[29] V.S. Bagotzky, Y.B. Vasilyev, Electrochim. Acta 9 (1964) 869.